Lee Yuni (Orcid ID: 0000-0003-0463-7650)
Dong Chuanfei (Orcid ID: 0000-0002-8990-094X)
Thiemann Edward, Michael Benjamin (Orcid ID: 0000-0002-5305-9466)
Mahaffy Paul, R. (Orcid ID: 0000-0003-1896-1726)
Benna Mehdi (Orcid ID: 0000-0002-2770-4820)
Combi Michael R. (Orcid ID: 0000-0002-9805-0078)
Bougher Stephen, W. (Orcid ID: 0000-0002-4178-2729)
Eparvier Francis, G. (Orcid ID: 0000-0001-7143-2730)

Effects of a Solar Flare on the Martian Hot O Corona and Photochemical Escape

Yuni Lee[1,2*], Chuanfei Dong[3], Dave Pawlowski[4], Edward Thiemann[5], Valeriy Tenishev[6], Paul

Mahaffy[1], Mehdi Benna[1,7], Michael Combi[6], Stephen Bougher[6], and Frank Eparvier[5]

[1]NASA Goddard Space Flight Center, Greenbelt, MD, USA

[2]GESTAR, Universities Space Research Association, Columbia, MD, USA

[3]Department of Astrophysical Sciences and Princeton Plasma Physics Laboratory, Princeton

University, Princeton, NJ, USA

[4]Department of Physics and Astronomy, Eastern Michigan University, Ypsilanti, MI, USA

[5]Laboratory for Atmospheric and Space Physics, University of Colorado, Boulder, CO, USA

[6]Climate and Space Sciences and Engineering Department, University of Michigan, Ann Arbor,

MI, USA

[7]CRESST II, University of Maryland, Baltimore, MD, USA

*Corresponding author: yuni.lee@nasa.gov

Manuscript prepared for submission to Geophysical Research Letters – Special issue

Abstract

We examine for the first time the flare-induced effects on the Martian hot O corona. The rapid ionospheric response to the increase in the soft X-ray flux (~800%) facilitates more hot O production at altitudes below the main ionospheric peak, but almost all of these atoms are thermalized before escape. In response to the increase in the EUV flux (~170%), the overall upper ionospheric and thermospheric densities are enhanced, and the peak thermospheric responses are found ~1.5 hours later. The photochemical escape rate is predicted to increase by ~20% with the increases in the soft X-ray and EUV fluxes but decrease rapidly by ~13% about 2.5 hour later before recovering the pre-flare level. Since escaping hot O atoms are mostly produced at high altitudes where ionization by the EUV flux is the greatest, the main contributor to the 20% increase in escape rate is the enhancement in the EUV flux.

1. Introduction

The Sun emitted an X8.2-class solar flare on 10 September 2017 from an active region, peaking at approximately 16:12 Universal Time (UT). Solar flares are massive bursts of energy from the Sun, covering the whole electromagnetic spectrum with increased radiation both in the extreme ultraviolet (EUV) and the X-ray wavelength regions. According to the NOAA flare scale, X-class flares are the most intense explosions on the Sun and can have a dramatic effect on the planetary atmospheres. Such brief and large enhancements produce a wide class of nonstationary influences on interplanetary plasma environments and planetary atmospheres and ionospheres. Physical processes at Earth induced by solar flares have been intensely investigated by various methods utilizing rich observation sets of the terrestrial ionosphere [*Thome and Wagner*, 1971; Davies, 1990; *Qian et al.*, 2011]. The solar flare effects in the atmosphere are characterized as inducing, for example, increased ionization in the upper atmosphere, which in

turn drastically enhances the ion and neutral densities, increased production of neutral species, and alteration of ionospheric composition [*e.g.*, *Mendillo and Evans*, 1974; *Le et al.*, 2007].

The Mars Atmosphere and Volatile EvolutioN (MAVEN) mission to Mars was launched in November 2013 and has been on its science mission for more than 1.5 Mars years. The primary goal of MAVEN is to study the physical and chemical processes controlling the escape of atmospheric constituents, the current state of the upper atmosphere, ionosphere, and magnetosphere of Mars, and their responses to the Sun and solar wind inputs [*Jakosky et al.*, 2015]. MAVEN has instrument packages that enabled comprehensive measurements of the atmosphere, ionosphere, and magnetosphere and the disturbed interplanetary conditions during the 10 September 2017 solar flare event.

While no previous study on effects on the neutral loss has been carried out, variability of photochemical escape of O for different solar activity levels and seasons has been investigated by a number of modeling studies [*e.g.*, *Cravens et al.*, 2017; *Fox and Ha*ć, 2009, 2014; *Gro*□*ller et al.*, 2014; *Lee et al.*, 2015b; *Lillis et al.*, 2017; *Rahmati et al.*, 2017; *Valeille et al.*, 2009a, 2009b; *Yagi et al.*, 2012]. The observed brightness of the hot O corona has shown strong correlation with changes in ionizing EUV flux, agreeing with the expectation that the primary source of hot O at Mars is dissociative recombination in the ionosphere [*Deighan et al.,* 2015].

We examine here for the first time the flare-induced effects on the hot O corona and subsequent photochemical loss of hot O by utilizing the integrated model framework. Our study

is designed to investigate the effects of the flare only and better capture the important atmospheric variability during the flare. This study presents (1) the effects on the formation of hot O corona by the 10 September 2017 solar flare and (2) the resulting variability of the hot O density and photochemical escape rates. We describe our models with their roles and input parameters in the integrated framework in section 2. A brief overview of the atmospheric and ionospheric conditions during the flare event using the Neutral Gas and Ion Mass Spectrometer (NGIMS) observations [*Mahaffy et al.*, 2014] and using our base model simulations are given in section 3. In section 4, we present our simulation results for the model cases considered and conclude in section 5.

2. Model Descriptions – Integrated Model Framework

2.1 AMPS / M-GITM / MF-MHD

The simulations in this study were conducted by integrating our 3D Adaptive Mesh Particle Simulator (AMPS) with the Mars Global Ionosphere Thermosphere Model (M-GITM) and the Multi-fluid Magnetohydrodynamic model (MF-MHD) in a one-way coupling framework to realistically model the effects of the solar flare on the photochemical escape process. AMPS, a state-of-the-art 3D Direct Simulation Monte Carlo (DSMC) model, is a kinetic particle model that employs a stochastic solver for both the linear and nonlinear Boltzmann equations. AMPS has been applied to a wide range of kinetic problems in rarefied gas flow including comets and planetary exospheres and served as a sophisticated and well-tested numerical model for studying

the physics of gas distribution in the tenuous planetary atmospheres. The full technical details of AMPS and its applications to the Martian exosphere can be found in *Tenishev et al.* [2008, 2013] and *Lee et al.* [2014a, 2014b, 2015a, 2015b]. To simulate the hot O corona, our AMPS code was run in a test-particle Monte Carlo mode instead of its full DSMC mode. The model particles move under the influence of the gravitational field of Mars and are traced until they escape or are thermalized in the computational domain.

The 3D M-GITM code [*Bougher et al.*, 2008, 2015; 2017], the base model of our integrated framework, is a 3D spherical model for Mars thermosphere and ionosphere developed based on the Earth GITM model [*Ridley et al.*, 2006]. Allowing the relaxation of the hydrostatic equilibrium assumption, the M-GITM code resolves the radial and horizontal fields separately and self-consistently solves the vertical continuity and momentum equations for each of the major neutral species. More details of M-GITM are outlined in *Bougher et al.* [2015]. For this study, a new M-GITM simulation has been made for the exact time period of the 10 September 2017 solar flare. New products from the Flare Irradiance Spectral Model for Mars (FISM-M) [*Chamberlin et al.*, 2007, 2008; *Thiemann et al.,* 2017] have been incorporated into the M-GITM code to provide global context for the impacts of the solar flare. FISM-M is tailored based on the observations by MAVEN Extreme Ultraviolet Monitor (EUVM) [*Eparvier et al.*, 2015]. This study uses flare irradiance estimates from *Thiemann et al.*, [2018], which improved the FISM-M irradiance estimates using additional algorithms and earth-based measurements. For each case considered, the thermosphere and ionosphere simulations were conducted on a 5º × 5º latitude

and longitude horizontal grid with a constant altitude resolution of 2.5 km from ~100 km to ~300 km, which is approximately equivalent to 0.25 scale height spacing, to provide neutral plus ion densities, temperatures (neutral, ion and electron) and neutral winds.

To incorporate detailed ion dynamics and chemical processes in the ionosphere, such as charge exchange, photoionization, and electron impact ionization, we employ the 3D BATS-R-US Mars MF-MHD model [*Najib et al.*, 2011; *Dong et al.*, 2014, 2015]. The Mars MF-MHD model contains a self-consistent ionosphere and thus the lower boundary is extended down to 100 km altitude above the planetary surface. We use an expansion of spherical harmonic functions up to degree and order 110 for the crustal magnetic field developed by *Morschhauser et al.* [2014]. To capture the ionospheric variations during the flare, we used the highest grid resolution so far in the MF-MHD calculations; the horizontal resolution is $1.5° \times 1.5°$ and the vertical resolution in the Martian ionosphere is ~3 km. We focus purely on the flare effect and filter the influence from the crustal field rotation and solar wind variations during the flare by fixing those parameters in the calculation. The crustal field location corresponds to 2017-09-10/17:42:16, which has subsolar longitude and subsolar latitude equal to -164.4° and 21.4°. The solar wind parameters are based on the average of the solar wind proxy during the flare [*Ma et al.*, 2018]: solar wind density $n_{sw}=7.0cm^{-3}$, solar wind velocity $U_x=314km/s$, and interplanetary magnetic field (nT) = (0.0,-2.5,0.0).

2.2. Model Integration and Study Cases

The model integration is carried out using a one-way method, such that one model uses pre-simulated results by an input provider model, where the feedback is not transferred back to the input provider model to update its computation. For the purpose of this study, we conducted an integrated one-way coupling procedure using AMPS, MF-MHD, and M-GITM. First, we performed a one-way coupling between AMPS and M-GITM, which has been achieved in our previous work for a nominal solar wind condition [*Lee et al.*, 2015b]. At this step, the hot O corona simulated by AMPS already includes the flare-induced effects. However, in order to include a more realistic description to the ionosphere, we performed a sub-coupling step by MF-MHD. In the current M-GITM version, the ions are static, which means the nascent ions do not have their momentum and energy equations to describe their dynamics. However, in MF-MHD, all the ion fluid dynamics are solved by the MF-MHD equations self-consistently. Therefore, the ions can be transported from dayside source region to the nightside, where nightside magnetic reconnection also makes contributions. The sub-coupling step performed by MF-MHD incorporates the hot O corona pre-computed by the AMPS and M-GITM coupling. Using the resulting MF-MHD's ionosphere and M-GITM's thermosphere, AMPS simulates the flare-induced effects on the hot O corona and photochemical escape process in a more realistic way.

All AMPS input parameters for collisional cross sections between hot O and thermospheric species are the same as described in *Lee et al.* [2015b] except for the total cross section for O_{hot}-$CO_{2,cold}$ collision ($2.0 \times 10^{-14} cm^2$). This study considers dissociative recombination (DR) of O_2^+ only as a source of hot O. Additional hot O can be created from other

nonthermal processes such as sputtering and other minor photochemical sources, which are not considered here. AMPS also takes into account the contribution from collisional source of hot O (*i.e.*, secondary hot O), which occurs when cold O (thermospheric O) gains enough energy to become hot O after colliding with hot O. This, in turn, implies that the production of secondary hot O is sensitive to the ambient thermospheric density variability in our simulations.

The flare-induced effects are examined by simulating the hot O corona for 4 time snapshots that represent the flare phases, namely, pre-flare, peak response for ionosphere and thermosphere, and post-flare: 10 September 15:02UT (pre-flare phase; case 1), 10 September 16:20UT (peak response phase for ionosphere; case 2), 10 September 18:45UT (peak response phase for thermosphere; case 3), and 11 September 12:00UT (post-flare phase; case 4).

3. Thermosphere and Ionosphere Conditions

3.1. A Brief Overview of the Temporal Variations Observed by NGIMS

During the flare, NGIMS made a set of ion and neutral measurements in the thermosphere and ionosphere. NGIMS samples ions on alternating orbits and neutrals on every orbit. The data presented in Figure 1 are from the inbound segments only in the level 2 data (v07_r01). When the flare occurred, the spacecraft was moving toward the smaller solar zenith angle (SZA) region from the near terminator region (from ~70° to 65°) at high latitudes. Based on the peak response times for the thermosphere and ionosphere estimated by M-GITM, the

NGIMS measurement for orbit 5718 can be roughly considered to be taken in the diminishing and enhancing phases of the ionospheric and thermospheric responses to the flare, respectively.

FIGURE 1

In response to the flare, the NGIMS observations show that the flare considerably affected the overall heating of the upper atmosphere [*Elrod et al.*, 2018]. Figure 1a shows the density profiles of the major thermospheric species, O and CO_2, measured by NGIMS. The pre-flare densities measurements indicate that the scale heights were approximately ~20 km and ~9 km, respectively. During the first post-flare measurement near 16:10UT (periapsis at 17:42UT), drastic heating in the upper atmosphere was observed, where the scale heights of O and CO_2 increased to ~34 km and ~13 km, respectively. The enhancement of the upper atmospheric temperature gradually decreased and recovered the pre-flare condition early in the morning on 11th (~01:01UT). At around 09:53UT on the 11th (periapsis at 11:26UT), the O density showed an enhancement by a factor of about 2 while the CO_2 density did not change.

The coupling signatures between the thermosphere and ionosphere are evident in the observations of the major ions. As shown in Figures 1b – 1d, about 1 hour after the flare, the observed electron density between ~180 km – 250 km is a factor of ~2 larger than the pre-flare measurements and decreased rapidly ~9 hours after the flare. The O_2^+, O^+, NO^+, and CO_2^+ densities showed a strong correlation in their densities with the O and CO_2 density during the

flare period as they are the parent species of the main production and loss reactions for the major ionospheric species. Especially, the enhancement in the NO^+ and O^+ densities at altitudes above ~200 km is larger than those of other species, which may roughly imply more sensitivity of the NO^+ and O^+ production to the variability of the solar soft X-ray flux. However, other sources of ion production are also possible such as heating in the thermosphere due to solar energetic particle precipitation, sputtering, or atmospheric wave heating.

3.2 Modeled Responses in the Thermosphere and Ionosphere

Figure 2a shows the modeled responses of the thermosphere and ionosphere to the solar flare that are relevant to the production and escape of hot O for our 4 model cases. The longitudinal and latitudinal distributions of the DR of O_2^+ rate are computed at an altitude of 180 km at which the escape probability of hot O reaches ~0.1 and the hot O density peaks. According to the case 2, the spatial structure of the DR of O_2^+ rate does not change significantly from pre-flare (case 1), but the magnitude of the rate shows a rapid enhancement. This enhancement is about ~43% at a SZA of ~20º at this particular altitude. At the altitude where the flare-induced escalation of electron density is maximized (~100 km), which is a factor of about 6.3 larger than the pre-flare level, the enhancement in hot O production also experiences its maximum. However, almost all of nascent hot O produced at this altitude region is found to be thermalized quickly due to the high collisional ambient environment. At the peak thermospheric response time (case 3), the DR rate decreases by ~14% with regard to case 2, but the ionosphere still produces ~23%

more hot O at the subsolar region than in case 1. After the soft X-ray and EUV irradiances completely recover the pre-flare level (case 4), the DR rate decreases by ~20% compared to case 3.

FIGURE 2

Figure 2b shows changes in spatial distribution of the neutral temperature at an altitude of ~200km for all 4 model cases. The neutral temperature starts increasing in case 2 from the pre-flare condition in case 1. Approximately 2.5 hours later, the maximum increase in the neutral temperature is achieved in case 3, which is ~245 K, peaking in the thermospheric response to the flare. The thermospheric density enhancement at this altitude region is approximately 22%, which ultimately has direct effects on the escape of hot O.

4. Responses of the Hot O Corona and Photochemical Escape
4.1. Variability of the Hot O Density

FIGURE 3

Figure 3 present the noon-midnight meridional plane views of the simulated hot O corona and relative increases in the hot O density in the Mars-Solar-Orbital (MSO) coordinate system.

During the flare, the season in the northern hemisphere of Mars was summer, and the solar activity level was close to its minimum. Throughout the model cases, the overall spatial structure of the coronal envelope does not change as the orbital position of Mars moves only about 0.5° during the event period, which lasted about a few hours. On the other hand, the magnitude of the hot O density increases rapidly as the flare begins to impact the atmosphere and ionosphere of Mars. In case 2, the enhancement in the dayside hot O density varies, ranging from ~15% to 45% over the pre-flare condition. The density decreases rapidly in case 3 when the thermospheric response peaks, which is about ~2.5 hours later, and recovers the pre-flare level in case 4 (~18 hours later). One of the main factors of the transient enhancement in the hot O density in case 2 is the rapid response of the ionosphere to the flare, which in turn increases the production of hot O. Furthermore, another factor is the time difference between thermospheric and ionospheric responses. If the peak response times for the thermosphere and ionosphere were almost simultaneous, then the enhanced hot O density would be quickly thermalized before escape to space. Thus, an efficient escape of the escalated hot O becomes possible due to the slower response of the thermosphere. In case 3, the hot O production is already in its diminishing phase, and the impeding of the hot O escape by the enhanced thermospheric density becomes maximized, causing a rapid decrease in escape rate.

4.2. Variability of Photochemical Escape

Figure 4 presents the solar soft X-ray and ionizing EUV irradiances observed by EUVM on 10-11 September 2017 as an indicator of the flare development. The soft X-ray irradiance started rising at 15:43UT, peaked at 16:12UT, and completely recovered the nominal condition at midnight. According to the observation, the X-ray and EUV irradiances were enhanced nearly by 800% and 170%, respectively. The subsequent panel in Figure 4 shows the computed photochemical escape rates for all 4 model cases considered in this study and the observed temporal variations in the exospheric temperature and exobase altitude, which are the derived products from the NGIMS L2 data (*i.e.*, NGIMS L3 data) based on the Ar density measurements.

FIGURE 4

As shown in Figure 4, the escape rate for the pre-flare case (case 1) increases by ~20% in case 2. The production of hot O increases with the X-ray irradiance in case 2, which is directly due to the increase in the electron density at altitudes below the main ionospheric peak [*e.g.*, *Medillo and Evans*, 1974; *Fox* 2004; *Lollo et al.*, 2012]. However, this enhancement at low altitudes is not likely to contribute to the total escape rate. The magnitude of the escape rate is more relevant to the production of hot O at altitudes where the collisional frequency is low enough for the escape of hot O (*i.e.*, above ~180km). Owing to the simultaneous increase in the EUV irradiance, the ionosphere at high altitudes is also enhanced, which in turn intensifies the

DR of O_2^+ rate. Thus, significant contribution to the 20% increase in escape rate is from the increased hot O production at high altitudes due to the enhanced EUV irradiance.

In case 3, where the peak thermospheric responses are seen, the escape rate decreased by ~10% and returns to the pre-flare level in the post-flare case (case 4). The decrease in escape rate in case 3 is attributed to (1) weakened hot O production rate due to the diminishing phase of the X-ray and EUV irradiance and (2) increase in the thermospheric density at ~200 km which induces more thermalization of hot O. According to the derived upper atmospheric quantities from the NGIMS measurements, the largest upper atmospheric temperature enhancement occurred at ~17:35UT and decreased to the pre-flare level in the next observation. The derived exobase altitude also peaked at ~233 km simultaneously with the temperature and decreased to a slightly lower altitude than the pre-flare level. Since this observation of the enhanced thermospheric response was taken about 1.5 hours later, it is possible that the maximum response in the upper atmospheric temperature and the exobase altitudes occurred near our model case 3, which is about 1 hour later. The overall thermospheric and ionospheric conditions recover the pre-flare condition in case 4, resulting in the similar escape rate.

5. Conclusion

This study presents for the first time the flare-induced effects on the hot O corona and photochemical escape using our integrated model framework. The effects described in this study are induced by input parameters derived only from the X8.2-class solar flare occurred on 10

September 2017. The simulations were conducted for 4 representative time snapshots for the flare phases. In order to fully incorporate and model the flare-induced effects, the input thermosphere and ionosphere for the AMPS model were carefully pre-simulated using the observation-based model parameters. The base model in our framework, M-GITM, described the thermosphere and ionosphere accordingly for the event period by incorporating spectral irradiance estimates based on solar radiation observations at Mars. The important ion dynamics were taken into account by adapting the solar wind information based on the solar wind proxy.

According to the major thermospheric species observed by NGIMS, the degree of the flare-induced effects was different for each species. Due to the coupling between neutrals and ions, the observed major ion densities also showed corresponding enhancements and rapidly restored to the pre-flare level. Our model estimates that the enhancement in hot O production reaches its maximum almost simultaneously with the flare peak, and that the maximum thermospheric density and temperature enhancement occurs ~2.5 hours later. Our simulated hot O corona shows that the overall intensification of the hot O density varies from ~15% to 45% in the dayside in case 2, without any significant changes in the spatial structure. As the thermalization increases due to the increased thermospheric response, the coronal density rapidly cools down in case 3 and returns to the pre-flare level in case 4.

The global escape rates via photochemical process from our integrated framework are 2.0×10^{25} s^{-1}, 2.4×10^{25} s^{-1}, 2.14×10^{25} s^{-1}, and 2.01×10^{25} s^{-1} for the case 1, 2, 3, and 4, respectively. The escape rate is enhanced by ~20% and ~7%, for case 2 and 3, respectively. For

case 2, the hot O production below the main ionospheric peak altitude is enhanced due to the escalated ionospheric densities by the increased X-ray flux. However, the main contributor to the increase in escape rate is the enhanced ionization in the upper atmosphere due to the increased EUV flux. Similarly, the effects of the EUV irradiance persists in case 3, but in diminishing phase, and the increase in the thermospheric densities at high altitudes brings another factor that reduces the escape rate by ~13% from case 2. The flare-induced effects are completely ceased in case 4, restoring to the pre-flare condition. This study demonstrates the flare-induced effects only on the photochemical escape rate, but there are other factors that can play a role in changing the escape rate such as solar cycle and seasonal variation [e.g., *Lee et al.*, 2015b; Cravens et al., 2017], which can induce a similar magnitude of variability.

References

Bougher, S. W., P.-L. Blelly, M. Combi, J. L. Fox, I. Mueller-Wodarg, A. Ridley, and R. G.

    Roble (2008), Neutral upper atmosphere and ionosphere modeling, *Space Sci. Rev.*,

    139,107–141, doi:10.1007/s11214-008-9401-9.

Bougher, S. W., D. J. Pawlowski, J. M. Bell, S. Nelli, T. McDunn, J. R. Murphy, M. Chizek, and

    A. Ridley (2015), Mars global ionosphere-thermosphere model (MGITM): Solar cycle,

    seasonal, and diurnal variations of the Mars upper atmosphere, *J. Geophys. Res*, 120,

    311–342, doi:10.1002/2014JE004715.

Bougher, S. W., K. Roeten, K. Olsen, P. R. Mahaffy, M. Benna, M. Elrod, S. K. Jain, N. M. Schneider, J. Deighan, E. Thiemann, F. G. Eparvier, A., Stiepen, and B. M. Jakosky, (2017). The structure and variability of Mars dayside thermosphere from MAVEN NGIMS and IUVS measurements: Seasonal and solar activity trends in scale heights and temperatures, *J. Geophys. Res. Space Physics*, 122, 1296-1313,doi:10.1002/2016JA023454.

Chamberlin, P. C., T. N. Woods, and F. G. Eparvier (2007), Flare Irradiance Spectral Model (FISM): Daily component algorithms and results, *Space Weather*, 5, S07005, doi:10.1029/2007SW000316.

Chamberlin, P. C., T. N. Woods, and F. G. Eparvier (2008), Flare Irradiance Spectral Model (FISM): Flare component algorithms and results, *Space Weather*, 6, S05001, doi:10.1029/2007SW00372.

Cravens, T. E., A. Rahmati, Jane L. Fox, R. Lillis, S. Bougher, J. Luhmann, S. Sakai, J. Deighan, Yuni Lee, M. Combi, and B. Jakosky (2017), Hot oxygen escape from Mars: Simple scaling with solar EUV irradiance, *J. Geophys. Res.*, 122, 1102, doi:10.1002/2016JA023461.

Davies, K (1990), *Ionospheric Radio*, Peter Peregrinus, London.

Dong, C. F., S.W. Bougher, Y.J. Ma, G. Toth, A.F. Nagy, and D. Najib (2014), Solar wind interaction with Mars upper atmosphere: Results from the one-way coupling between the

multi-fluid MHD model and the M-TGCM model, *Geophys. Res. Lett.*, 41, 2708-2715, doi:10.1002/2014GL059515.

Dong, C. F., S.W. Bougher, Y.J. Ma, G. Toth, Y. Lee, A.F. Nagy, V. Tenishev, D.J. Pawlowski, M.R. Combi, and D. Najib (2015), Solar wind interaction with the Martian upper atmosphere: Crustal field orientation, solar cycle and seasonal variations, *J. Geophys. Res. Space Physics,* 120, 7857-7872, doi:10.1002/2015JA020990.

Elrod, M., et al. (2018), September 2017 Solar Flare Event: Rapid Heating of the Martian Neutral Thermosphere from the X-class flare as observed by MAVEN, *Geophys. Res. Lett.*, 2018GL077729, this issue.

Eparvier, F. G., Chamberlin, P. C., Woods, T. N., & Thiemann, E. M. B. (2015). The solar extreme ultraviolet monitor for MAVEN. Space Science Reviews, 195(1-4), 293-301.

Fox, J. L. (2004), Response of the Martian thermosphere/ionosphere to enhanced fluxes of solar soft X rays, *J. Geophys. Res.*, 109, A11310, doi:10.1029/2004JA010380.

Jakosky, B. M., R. P. Lin, J. M. Grebowksy, J. G. Luhmann, and others (2015), The Mars Atmosphere and Volatile Evolution (MAVEN) Mission, *Space Sci. Reviews*, 195, 3–48, doi:10.1007/s11214- 015-0139-x.

Le, H., L. Liu, B. Chen, J. Lei, X. Yue, and W. Wan (2007), Modeling the responses of the middle latitude ionosphere to solar flares, *J. Atmos. Sol. Terr. Phys.*, 69, 1587-1598, doi:10.1016/j.jastp.2007.06.005.

Lee, Y., et al. (2015a), A comparison of 3-D model predictions of Mars' oxygen corona with early MAVEN IUVS observations, *Geophys. Res. Lett.*, 42, doi:10.1002/2015GL065291.

Lee, Y., M. R. Combi, V. Tenishev, and S. W. Bougher (2014a), Hot carbon corona in Mars' upper thermosphere and exosphere: 1. Mechanisms and structure of the hot corona for low solar activity at equinox, *J. Geophys. Res. Planets*, 119, 905–924, doi:10.1002/2013JE004552.

Lee, Y., M. R. Combi, V. Tenishev, and S. W. Bougher (2014b), Hot carbon corona in Mars' upper thermosphere and exosphere: 2. Solar cycle and seasonal variability, *J. Geophys. Res. Planets*, 119, 2487–2509, doi:10.1002/2014JE004669.

Lee, Y., M. R. Combi, V. Tenishev, S. W. Bougher, and R. J. Lillis (2015b), Hot oxygen corona at Mars and the photochemical escape of oxygen: Improved description of the thermosphere, ionosphere, and exosphere, *J. Geophys. Res. Planets*, 120, 1880–1892, doi:10.1002/2015JE004890.

Lillis, R. J., J. Deighan, Jane Fox, S. Bougher, Y. Lee, M. Combi, T. E. Cravens, Ali Rahmati, P. Mahaffy, et al. (2017), Photochemical escape of oxygen from Mars: First results from MAVEN in situ data, *J. Geophys. Res.*, 122, 3815-3836, doi:10.1002/2016JA023525.

Lollo, A., P. Withers, K. Fallows, Z. Girazian, M. Matta, and P. C. Chamberlin (2012), Numerical simulations of the ionosphere of Mars during a solar flare, *J. Geophys. Res.*, 117, A05314, doi:10.1029/2011JA017399.

Ma, Y., et al. (2018), The Impact and Solar wind Proxy of the 2017 September ICME Event at Mars, Geophys. Res. Lett., 2018GL077707, this issue.

Mahaffy, P. R., et al. (2014), The neutral gas and ion mass spectrometer on the Mars atmosphere and volatile evolution mission, *Space Sci. Rev.*, 195(1), 49–73, doi:10.1007/s11214-014-0091-1.

Mendillo, M., and J. V. Evans (1974), Incoherent scatter observations of the ionospheric response to a large solar flare, *Radio Sci.*, 9, 197-203, doi:10.1029/RS009i002p00197.

Morschhauser, A., V. Lesur, and M. Grott (2014), A spherical harmonic model of the lithospheric magnetic field of Mars, *J. Geophys. Res. Planets*, 119, 1162–1188, doi:10.1002/2013JE004555.

Najib, D., A. F. Nagy, G. Toth, Y.J. Ma (2011), Three-dimensional, multifluid, high spatial resolution MHD model studies of the solar wind interaction with Mars, *J. Geophys. Res. Space Physics*, 116, A05204, doi:10.1029/2010JA016272.

Qian, L., Burns, A. G., Chamberlin, P. C., & Solomon, S. C. (2011). Variability of thermosphere and ionosphere responses to solar flares. *J. Geophys. Res. Space Physics*, *116*(A10).

Rahmati, A., D. E. Larson, T. E. Cravens, R. J. Lillis, J. S. Halekas, J. P. McFadden, P. A. Dunn, D. L. Mitchell, E. M. B. Thiemann, F. G. Eparvier, G. A. DiBraccio, J. R. Espley, C. Mazelle, and B. M. Jakosky (2017), MAVEN measured oxygen and hydrogen pickup ions: Probing the Martian exosphere and neutral escape, *J. Geophys. Res.*, 122, 3689, doi:10.1002/2016JA023371.

Ridley, A. J., Y. Deng, and G. Toth (2006), The global ionosphere-thermosphere model. *J. Atmos. Sol-Terr. Phys.*, 68, 839.

Tenishev, V., M. R. Combi, and B. Davidsson (2008), A Global kinetic model for cometary comae. The evolution of the coma of the Rosetta target comet Churyumov–Gerasimenko throughout the mission, *Astrophys. J.*, 685, 659–677.

Tenishev, V., M. Rubin, O. J. Tucker, M. R. Combi, and M. Sarantos (2013), Kinetic modeling of sodium in the lunar exosphere, Icarus, 226, 1538–1549, doi:10.1016/j.icarus.2013.08.021.

Thiemann, E., Chamberlin, P. C., Eparvier, F. G., Templeman, B., Woods, T. N., Bougher, S. W., & Jakosky, B. M. (2017). The MAVEN EUVM model of solar spectral irradiance variability at Mars: Algorithms and results, *J. Geophys. Res. Space Physics*, *122*(3), 2748-2767.

Thiemann, E.M.B., Andersson, L.A., Lillis, R., Withers, P., Xu, S., Elrod, M.,Pawlowski, D., Chamberlin, P.C., Eparvier, F.G., Benna, M., Fowler, C., Pilinksi, M.D., Curry, S. (2018) The Mars Upper Ionosphere Response to the X8.2 Solar Flare of 10 September 2017. *Geophys. Res. Lett.*, 2018GL077730, this issue.

Thome, G. D., and L. S. Wagner (1971), Electron density enhancements in the E- and F-regions of the ionosphere during solar flares, *J. Geophys. Res.*, 76, 6883-6895.

Yagi, M., F. Leblanc, J. Y. Chaufray, F. Gonzalez-Galindo, S. Hess, and R. Modolo (2012), Mars exospheric thermal and non-thermal components: Seasonal and local variations, *Icarus*, 221, 682–693.
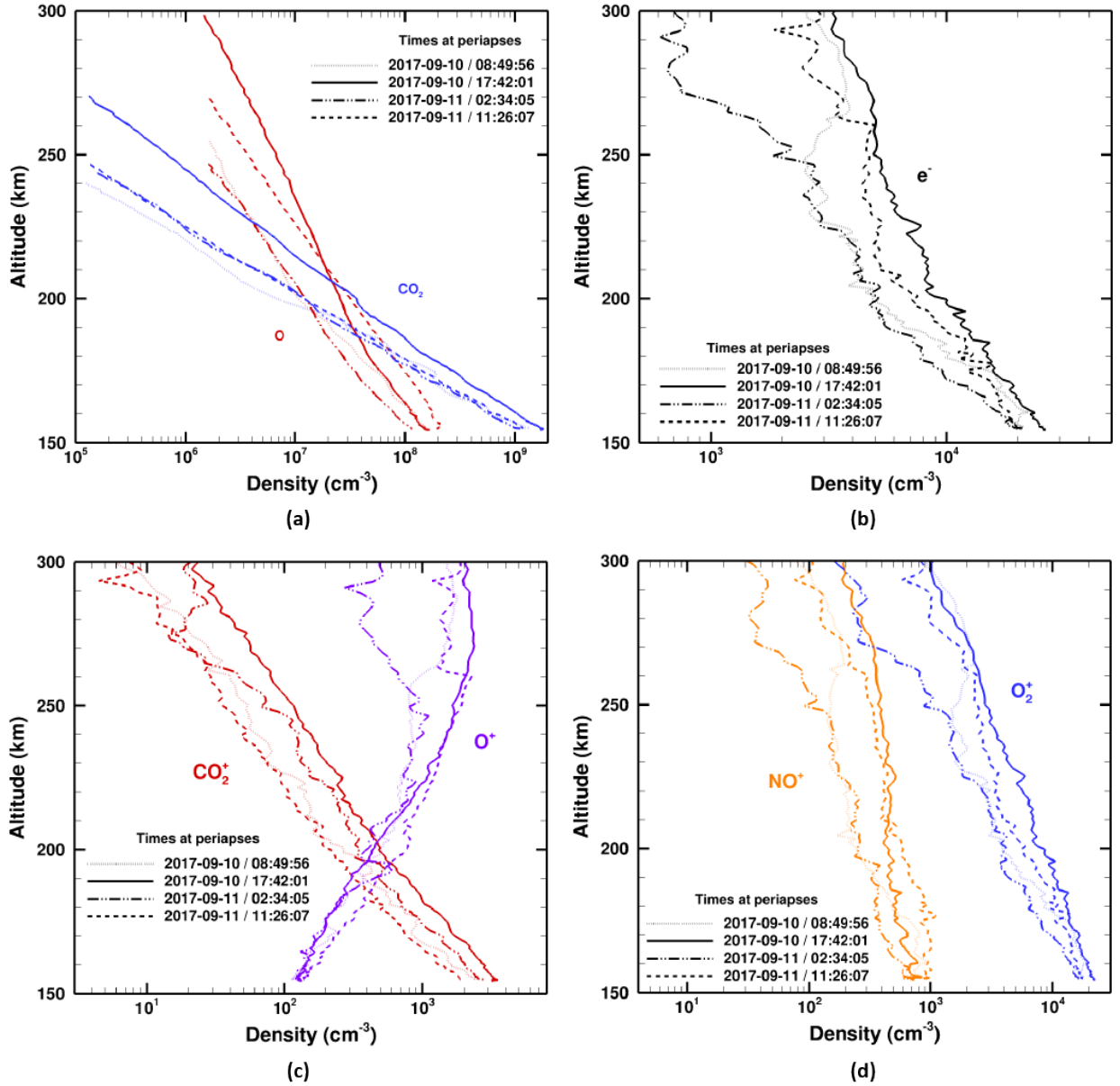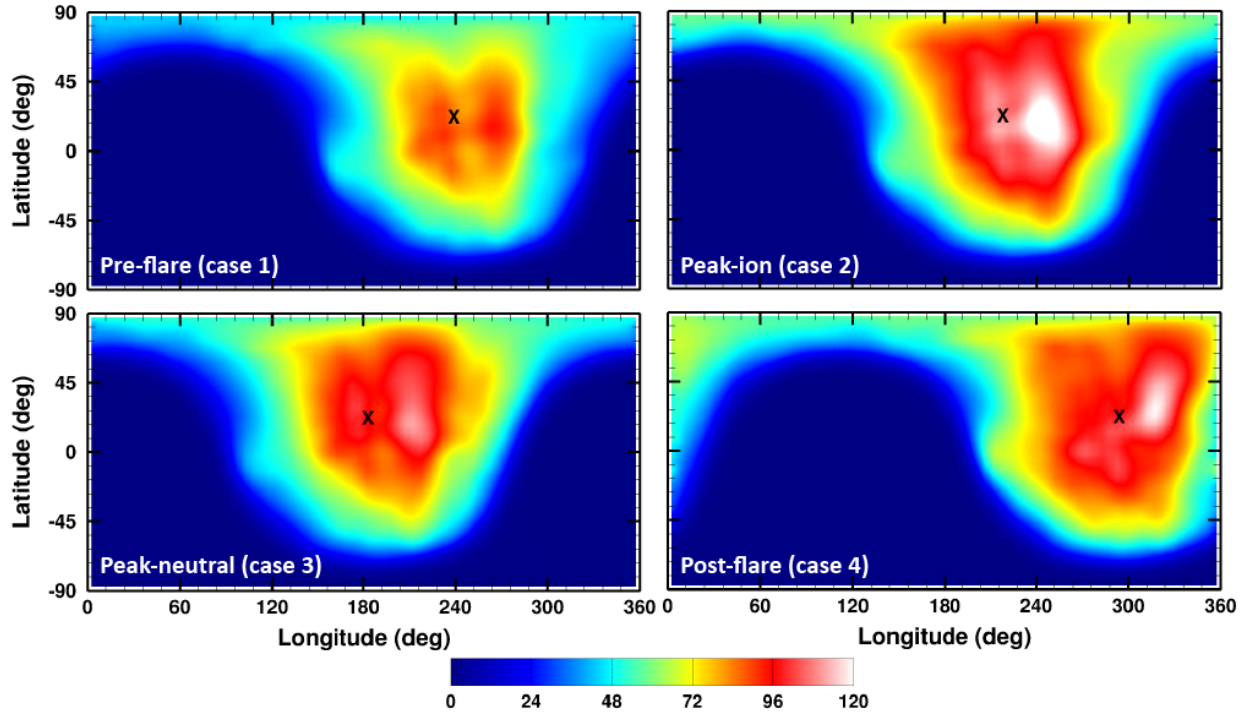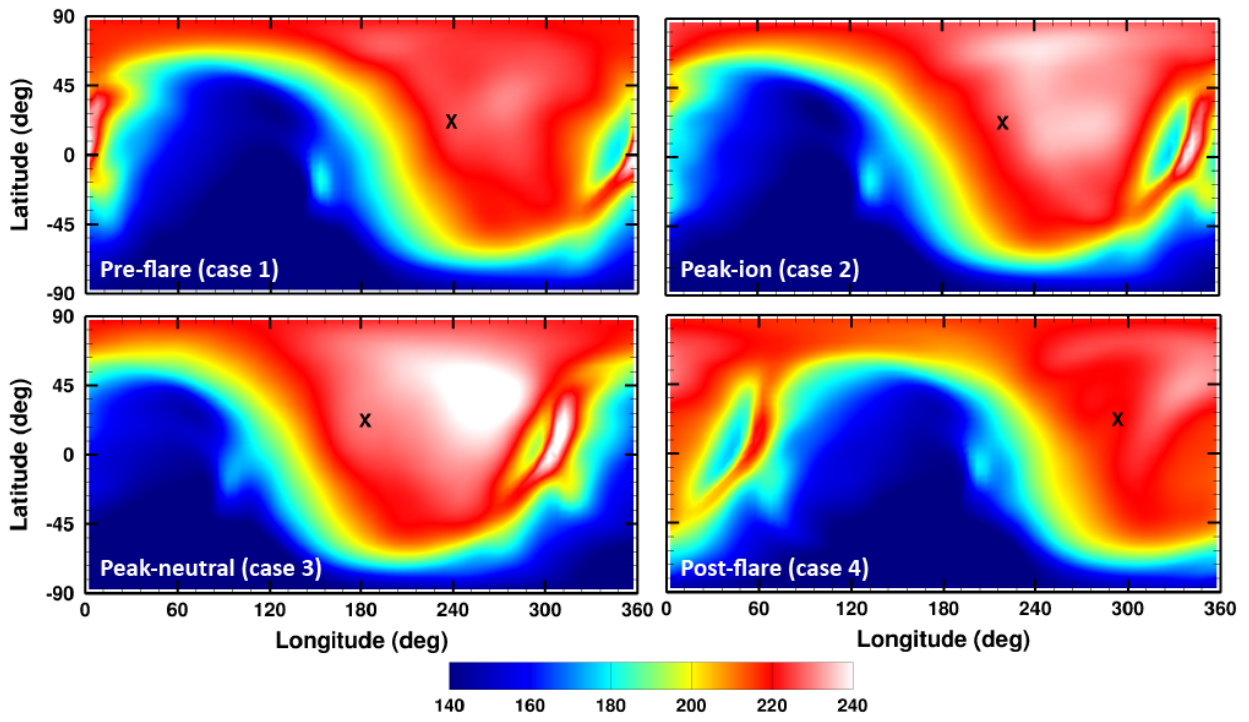
Figure 1. NGIMS observations of the major neutrals and ions during the flare. (a) O and CO_2, (b) electron obtained by summing all ions, (c) CO_2^+ and O^+, and (d) NO^+ and O_2^+.

(a)

(b)

Figure 2. Longitudinal and latitudinal distributions of (a) DR of O_2^+ rate in $cm^{-3}s^{-1}$ at 180 km and (b) neutral temperature in K at 200 km. The longitude is east longitude. For both (a) and (b), case 1, 2, 3, and 4 are top left, top right, bottom left, and bottom right, respectively. "X" mark indicates the subsolar location.
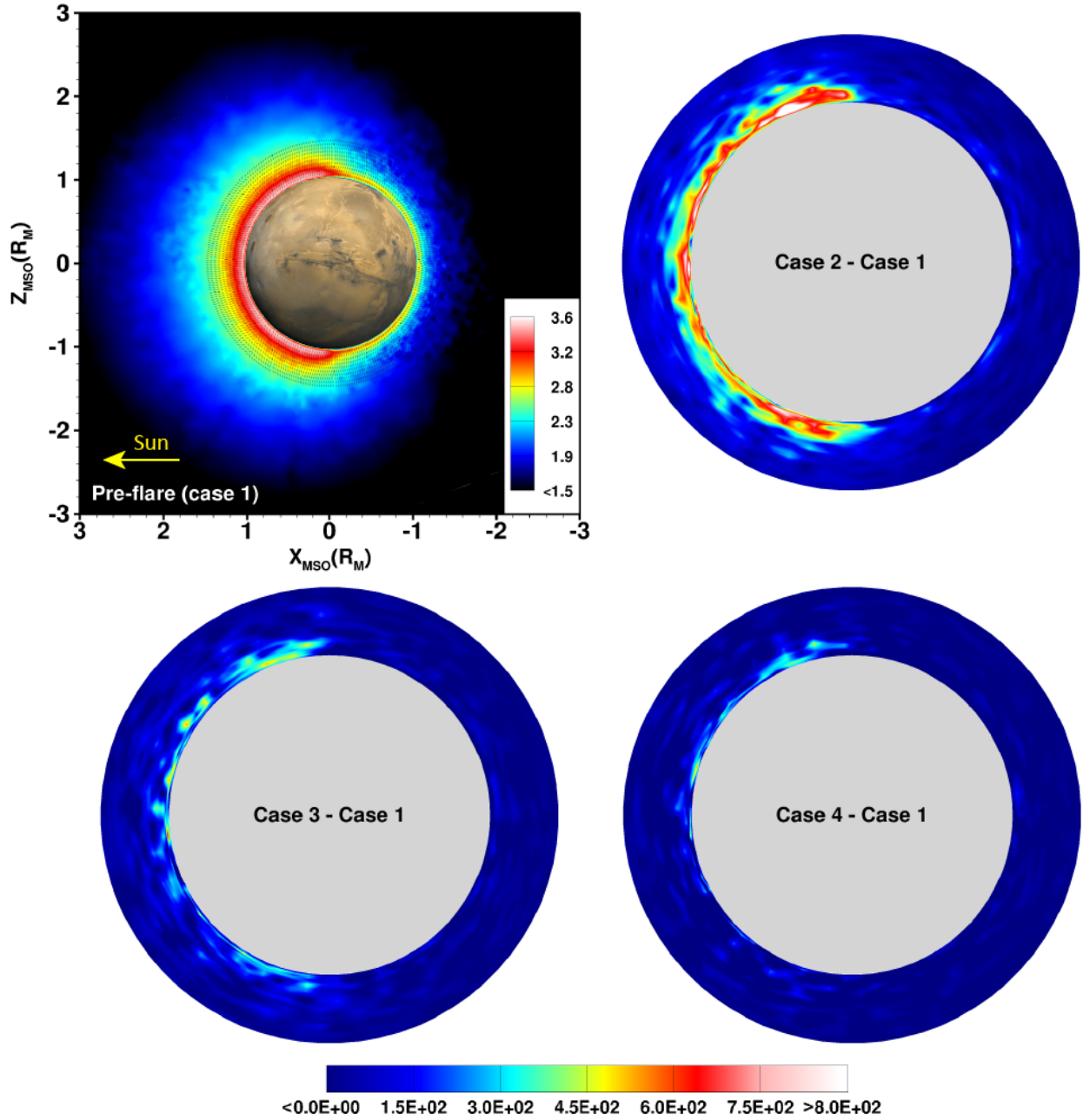
Figure 3. (left column) The noon-midnight meridional plane view of the simulated hot O corona in the MSO coordinate system. The color contour indicates the log of the hot O density (cm^{-3}).

Case 1, 2, 3 and 4 are from top to bottom, respectively. (right column) Differences in number

densities (cm^{-3}) between flare-impacted cases (case 2, 3, and 4) and case 1 from the surface of
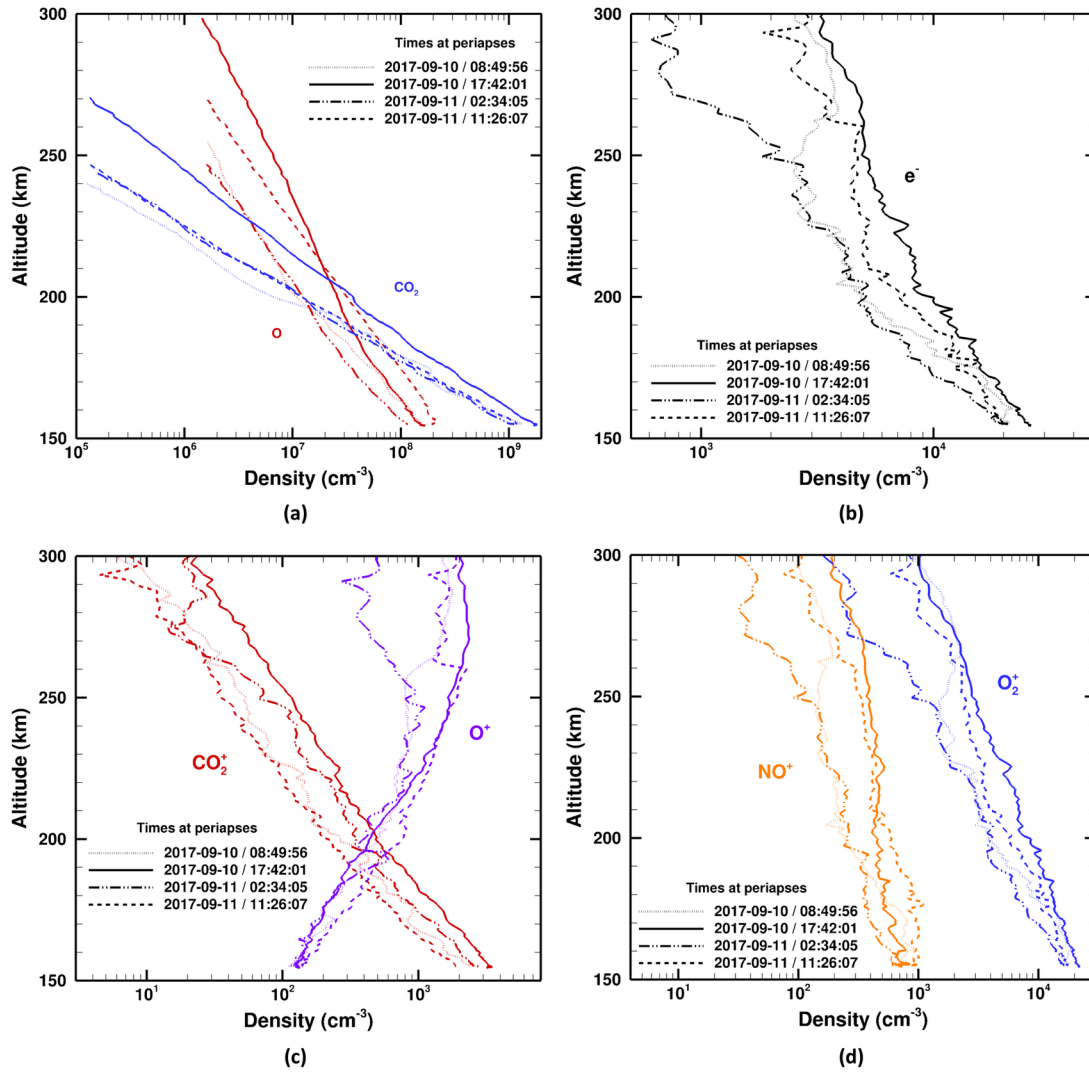
the planet to ~1500 km.
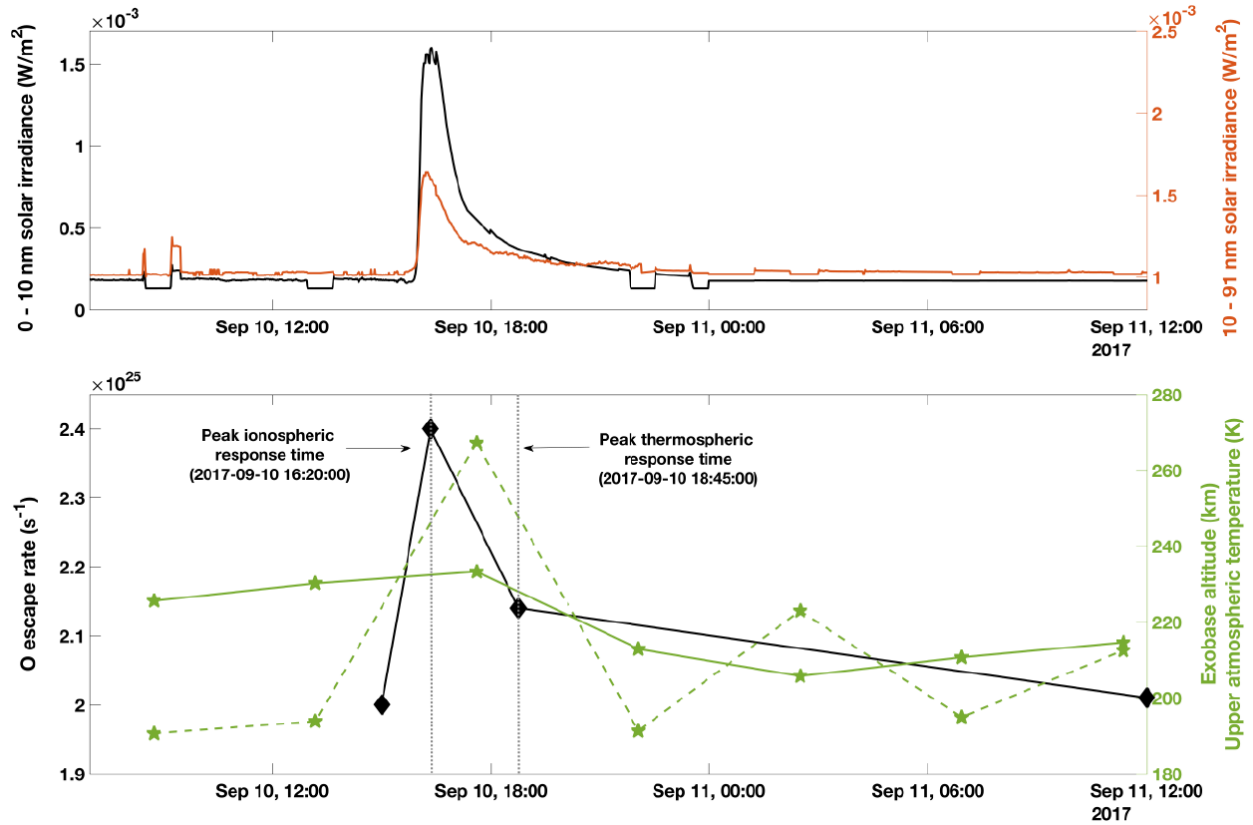
Figure 4. Temporal variations in the ionizing EUV (red) and soft X-ray irradiances (black) in the

top panel, and computed photochemical escape rates (black), exobase altitude (green-solid), and

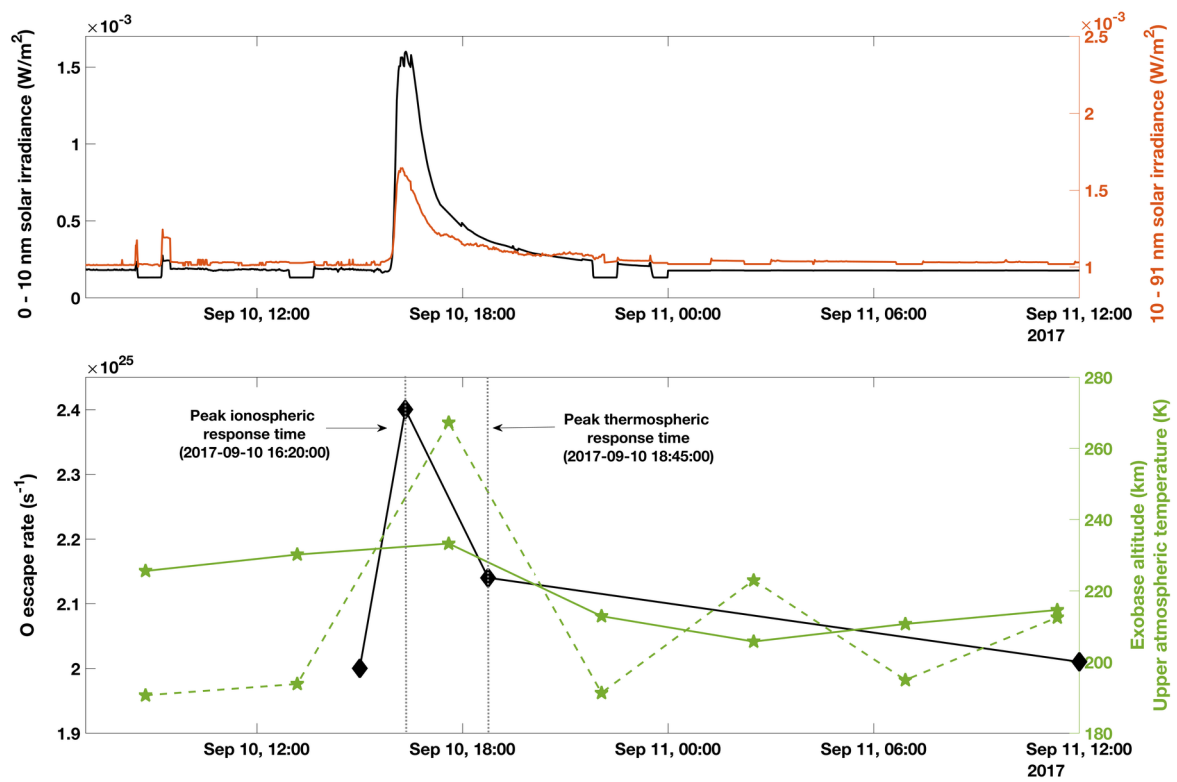upper atmospheric temperature (green-dash) in the bottom panel.

2018GL077732-f01-z-.tif

(a)

(b)

2018GL077732-f02-z-.tif

Pre-flare (case 1)

Sun

Case 2 - Case 1

Case 3 - Case 1

Case 4 - Case 1
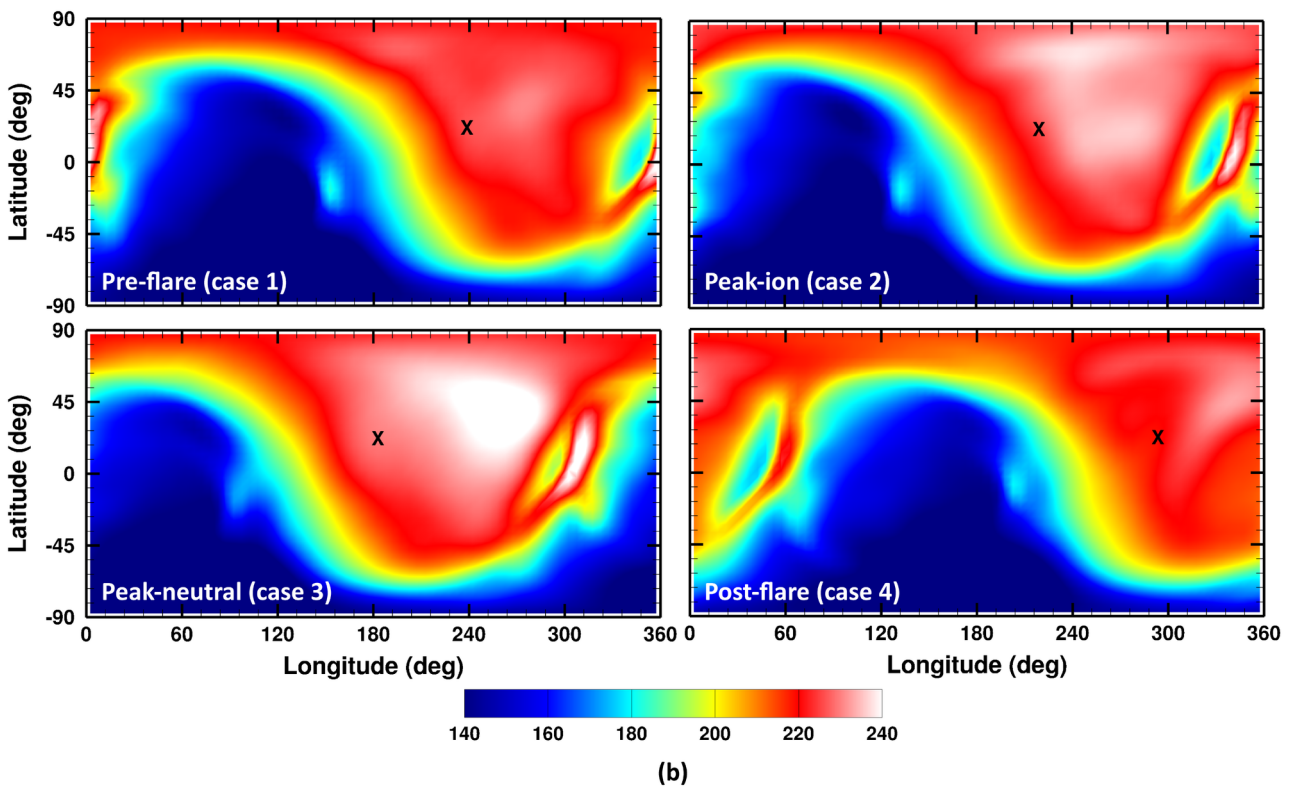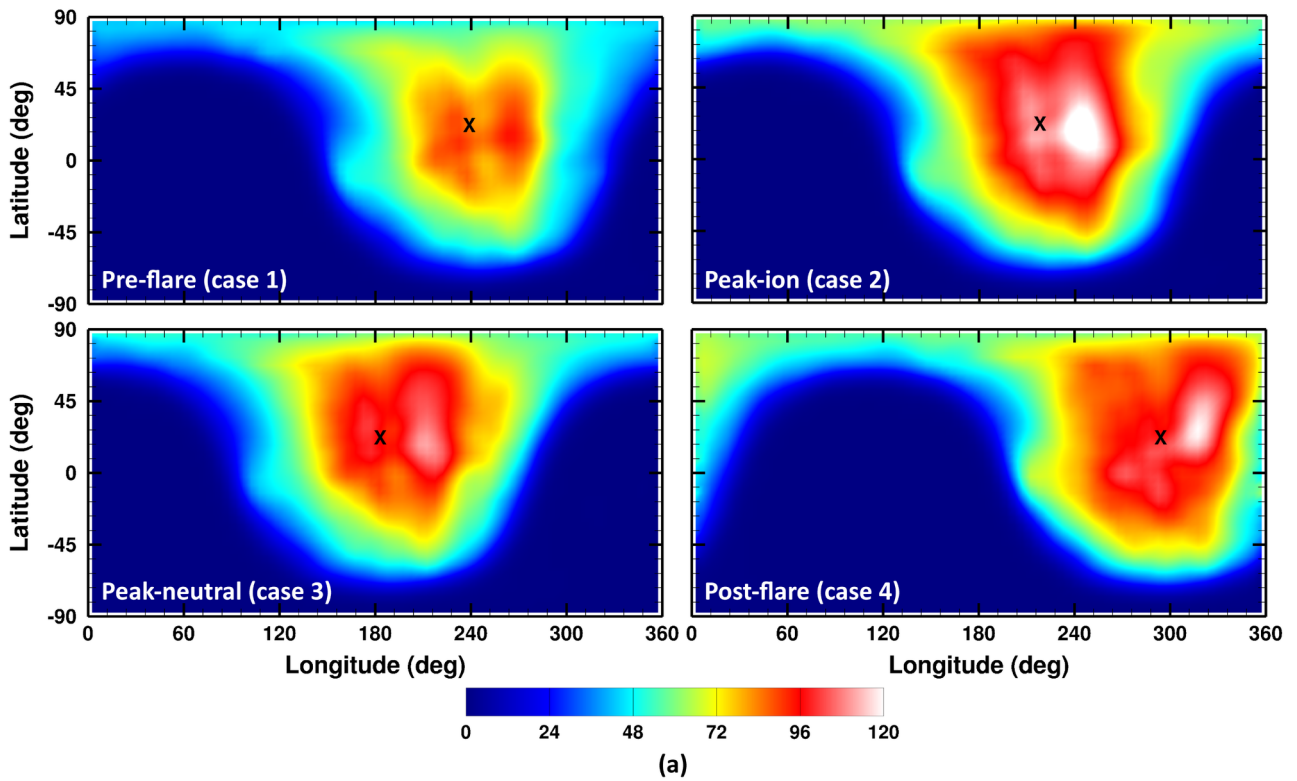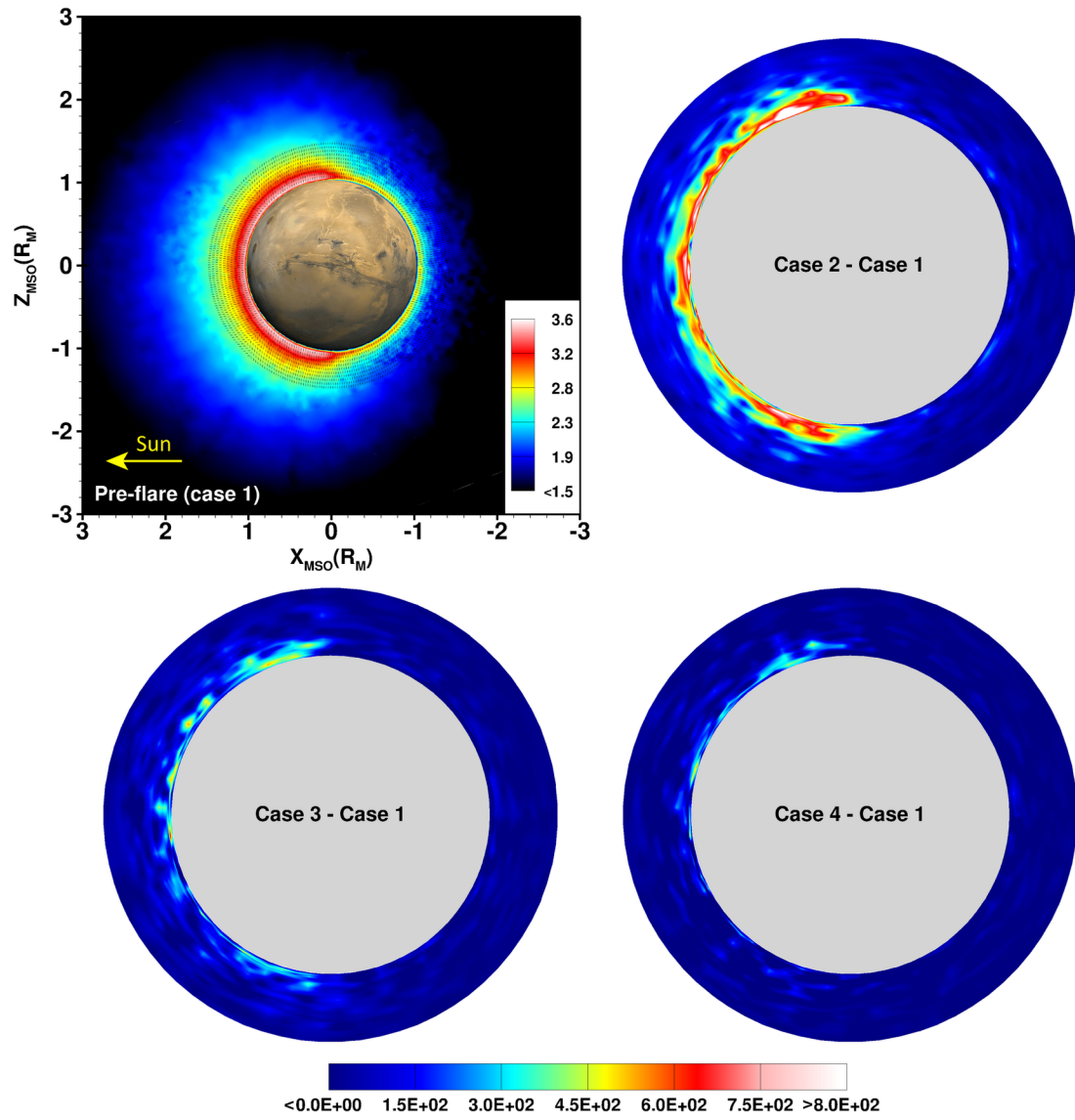
2018GL077732-f03-z-.tif

2018GL077732-f04-z-.tif